Trimodal structure of Hercules stream explained by originating from bar resonances

Tetsuro Asano [1][*] M. S. Fujii [1] J. Baba,[2] J. Bédorf,[3,4] E. Sellentin[3] and S. Portegies Zwart[3]

[1]*Department of Astronomy, Graduate School of Science, The University of Tokyo, 7-3-1 Hongo, Bunkyo-ku, Tokyo 113-0033, Japan*
[2]*National Astronomical Observatory of Japan, Mitaka-shi, Tokyo 181-8588, Japan*
[3]*Leiden Observatory, Leiden University, NL-2300RA Leiden, The Netherlands*
[4]*Minds.ai, Inc., Santa Cruz, CA 95060, USA*

ABSTRACT

Gaia Data Release 2 revealed detailed structures of nearby stars in phase space. These include the Hercules stream, whose origin is still debated. Most of the previous numerical studies conjectured that the observed structures originate from orbits in resonance with the bar, based on static potential models for the Milky Way. We, in contrast, approach the problem via a self-consistent, dynamic, and morphologically well-resolved model, namely a full *N*-body simulation of the Milky Way. Our simulation comprises about 5.1 billion particles in the galactic stellar bulge, bar, disc, and dark-matter halo and is evolved to 10 Gyr. Our model's disc component is composed of 200 million particles, and its simulation snapshots are stored every 10 Myr, enabling us to resolve and classify resonant orbits of representative samples of stars. After choosing the Sun's position in the simulation, we compare the distribution of stars in its neighbourhood with *Gaia*'s astrometric data, thereby establishing the role of identified resonantly trapped stars in the formation of Hercules-like structures. From our orbital spectral-analysis, we identify multiple, especially higher order resonances. Our results suggest that the Hercules stream is dominated by the 4:1 and 5:1 outer Lindblad and corotation resonances. In total, this yields a trimodal structure of the Hercules stream. From the relation between resonances and ridges in phase space, our model favoured a slow pattern speed of the Milky-Way bar (40–45 km s^{-1} kpc^{-1}).

Key words: methods: numerical – Galaxy: disc – Galaxy: kinematics and dynamics – solar neighbourhood – Galaxy: structure.

1 INTRODUCTION

The European Space Agency (ESA) is operating an astrometric mission *Gaia* (Gaia Collaboration et al. 2016), which observed our Milky Way (MW). Its second data release (*Gaia* DR2; Gaia Collaboration et al. 2018a) provides five astrometric parameters for 1.3 billion sources and additional line-of-sight velocities for 7.2 million sources. For stars, these astrometric data provide snapshots of their orbits in the Galactic potential and we here aim to obtain information on the dynamical structure of the MW by investigating the phase-space distributions of its stars. In this context, velocity–space structures of the solar neighbourhood have previously been repeatedly studied (e.g. Kalnajs 1991; Dehnen 1998, 1999), but mainly under analytical or numerical approximations which we here drop.

In Fig. 1, we present the distribution of radial velocities, v_R, versus angular velocities, v_ϕ, of stars observed with *Gaia* (similar to fig. 22 in Gaia Collaboration et al. 2018b). In this map, we see several arch-shaped overdensities with such as the so-called 'horn' near $(v_R, v_\phi) \sim (-50, 220)$ km s^{-1} (Monari et al. 2017a; Fragkoudi et al. 2019) and the so-called 'hat' near $(v_R, v_\phi) \simeq (\pm 50, > 250)$ km s^{-1} (e.g. Hunt & Bovy 2018; Hunt et al. 2019). The most prominent

structure is called the 'Hercules' stream, and is located between $(v_R, v_\phi) \simeq (100, 200)$ km s^{-1} and $(v_R, v_\phi) \simeq (-70, 170)$ km s^{-1}.

Dehnen (1998) originally identified the Hercules stream as *U*-anomaly from the *Hipparcos* data (ESA 1997; Perryman et al. 1997), and *Gaia* DR2 (Gaia Collaboration et al. 2018a,b) revealed further detailed structures within. *Gaia* DR2 showed for the first time the trimodal structure of the Hercules stream, which is composed of three sub-streams at $v_\phi \simeq 220$, 200, and 180 km s^{-1} (Ramos, Antoja & Figueras 2018; Gaia Collaboration et al. 2018b; Trick, Coronado & Rix 2019; Li & Shen 2020). Although we refer to the bottom stream in Fig. 1 as 'Hercules 3', it is identical to a moving group, HR 1614 (Eggen 1971, 1978; Kushniruk et al. 2020).

Soon after the first discovery of the Hercules stream, a scenario on its origin was proposed by Dehnen (1999), (2000). He calculated the evolution of the stellar phase-space distribution in the simple $m = 2$ bar potential (where m indicates the azimuthal Fourier mode), and then argued that stars trapped in the 2:1 outer Lindblad resonance (OLR) of the bar can create moving groups in the solar neighbourhood. The exact position of the formed structure in phase space depends on the location of the OLR and the OLR position depends in turn on the pattern speed of the bar (Ω_b). Hence, to reproduce the observed features, this scenario requires a fast rotating bar to bring the 2:1 OLR around 8 kpc, i.e. $\Omega_b/\Omega_0 = 1.85$ (where Ω_0 is the local circular frequency); this corresponds to $\Omega_b = 53 \pm 3$ km s^{-1}kpc^{-1}

[*] E-mail: t.asano@astron.s.u-tokyo.ac.jp

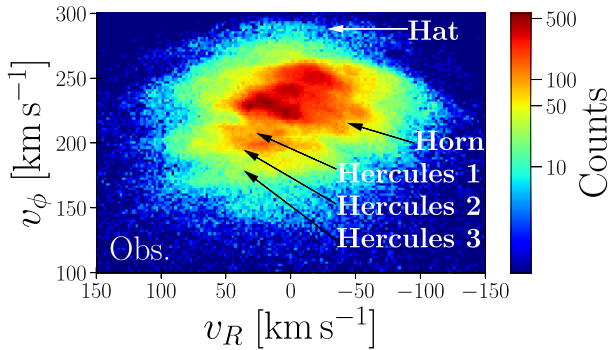**Figure 1.** Radial and angular velocity–space distribution of stars within 0.2 kpc from the Sun, binned by $2 \times 2 \, (\mathrm{km \, s^{-1}})^2$. From *Gaia* DR2 catalogue, we selected stars whose relative errors in parallax are smaller than 10 per cent.

(see also Fux 2001; Minchev, Nordhaus & Quillen 2007; Minchev et al. 2010; Antoja et al. 2014). Such a fast ($\Omega_b \sim 50 \, \mathrm{km \, s^{-1} kpc^{-1}}$) bar model is also favoured by test particle integration in a more realistic MW Galaxy potential that was constructed from an *N*-body simulation (Fragkoudi et al. 2019).

On the other hand, recent observations suggest slower pattern speeds of the bar. Combining data from *Gaia* DR2 and further surveys, both Sanders, Smith & Evans (2019) and Bovy et al. (2019) estimated a pattern speed of $\Omega_b = 41 \pm 3 \, \mathrm{km \, s^{-1} \, kpc^{-1}}$, and Clarke et al. (2019) estimated $\Omega_b = 37.5 \, \mathrm{km \, s^{-1} \, kpc^{-1}}$. Recent measurements of the bar length also support a slow bar model. The measured ratio of the corotaion radius (R_{CR}) to the bar length (R_b) $R_{CR}/R_b = 1.2 \pm 0.2$ for external galaxies (Aguerri, Debattista & Corsini 2003; Aguerri et al. 2015). The bar length of $R_b = 5.0 \pm 0.2$ kpc in the MW (Wegg, Gerhard & Portail 2015) therefore suggests the corotation radius of $R_{CR} \simeq 5$–7 kpc or the pattern speed of $\Omega_b \simeq 34$–$47 \, \mathrm{km \, s^{-1} \, kpc^{-1}}$. In addition, such slow and long bar is also supported by the dynamical modelling of bulge stars (Portail et al. 2017) and gas kinematics (Sormani, Binney & Magorrian 2015; Li et al. 2016). With such a slow pattern speed, the 2:1 OLR should be located further than 8 kpc.

The slow and long bar model enhanced the studies of the Hercules stream's origin, and new scenarios have been suggested. Most of them agree with the concept that resonant orbits due to non-axisymmetric structures, such as a bar and/or spiral arms, create the moving groups in the solar neighbourhood revealed by *Gaia* DR2. One of the new scenarios is the bar's corotation (CR) scenario. Pérez-Villegas et al. (2017) integrated orbits of test particles in a gravitational field constructed from a self-consistent *N*-body model of the MW to match observational data using the Made-to-Measure (M2M) method (Portail et al. 2017), and then proposed that the Hercules-like stream can be made of stars orbiting around Lagrangian points of the bar. These stars move outwards from the bar's CR radius to visit the solar neighbourhood. In this study, they assumed a slow bar ($\Omega_b \sim 40 \, \mathrm{km \, s^{-1} \, kpc^{-1}}$). This scenario is also supported by analytic calculations of perturbed distribution functions in resonance regions (Monari et al. 2019a,b; Binney 2020) and full *N*-body simulations of a MW-like galaxy (D'Onghia & L. Aguerri 2020).

Another new scenario attributes the Hercules stream to higher order resonances of the slow, long bar. Hunt & Bovy (2018) integrated orbits of test particles in analytic bar potentials including an $m = 4$ Fourier mode and suggested that the 4:1 OLR of a slowly rotating bar can lead to a bi-modal structure in the Hercules stream. Monari et al. (2019a) also studied the relation between the bar's higher order resonances and the solar neighbourhood kinematics using a resonant

distribution function model (Monari et al. 2017c) in the same realistic bar potential as that used in Pérez-Villegas et al. (2017). They showed that CR and 6:1 OLR of the bar create a Hercules-like stream and a horn-like structure, respectively. Similarly, Michtchenko et al. (2018) performed test particle simulations in a slow-bar potential with higher-order multipole moments combined with a spiral potential and suggested that the Hercules stream associated with the spiral's 8:1 ILR (see also Barros et al. 2020). On the other hand, Hattori et al. (2019) also showed that Hercules-like streams originate from orbit families associated with the 5:1 inner Lindblad resonance (ILR) in the simple $m = 2$ slow-bar + spiral potentials.

Note that most of the above studies are based on test particle simulations in 'static' (or analytic) potentials. We can easily capture resonant orbits of stars in static potentials; however, previously performed self-consistent *N*-body simulations of (barred) spiral galaxies have suggested that the structures in the spiral arms and bar change with time in complicated ways (e.g. Sellwood & Carlberg 1984; Sellwood & Sparke 1988; Baba et al. 2009; Fujii et al. 2011; Grand, Kawata & Cropper 2012a, b; Baba, Saitoh & Wada 2013; D'Onghia, Vogelsberger & Hernquist 2013; Khoperskov et al. 2019). Such transient nature may affect stellar orbits in higher order resonances. Higher order resonances are usually weaker than CR or 2:1 OLR. In order to detect higher order resonances such as 4:1 and 6:1 OLR in self-consistent *N*-body simulations, a high enough resolution is required. Recently, D'Onghia & L. Aguerri (2020) captured stars in the CR resonance using fully self-consistent *N*-body simulations, but they did not report higher order resonances as the origins of the Hercules stream. Hence, so far no high-order resonances have been reported in self-consistent *N*-body simulations.

Phase-space structures have been found in these self-consistent *N*-body models, but their origin is unknown. Fujii et al. (2019) performed *N*-body simulations of disc galaxy models and found a MW-like model, of which some observed structures and kinematics match those of the MW. They performed simulations using a maximum of 8 billion particles (more than 200 million particles for the disc) with the dark-matter halo modelled with *N*-body particles (live halo). This is an order of magnitude higher mass-resolution than previous similar studies (e.g. D'Onghia & L. Aguerri 2020). Fujii et al. (2019) showed *U*–*V* maps obtained in their simulations and discussed if Hercules-like streams are found in *N*-body simulations. Indeed, they found some Hercules stream-like structures in their simulations, but the origin of the structures has not been investigated.

In this paper, we analyse the results of the *N*-body simulations performed in Fujii et al. (2019), which represents an isolated MW-like galaxy modelled completely as an *N*-body system. In this simulation, we track and classify the stellar orbits. The purpose of the classification is to identify stars trapped in resonance. We then show that stars trapped in higher order resonances actually exist in the live disc potential and that the trimodal structure of the Hercules stream can be explained by such higher order resonances.

2 MW *N*-BODY SIMULATIONS

2.1 Initial condition and dynamical evolution of the MW model

We use one of the MW *N*-body simulations that were performed by Fujii et al. (2019). Here, we describe their model and simulation methods.

We use model MWa of Fujii et al. (2019). This model is an MW-like galaxy composed of a live stellar disc, a live classical bulge, and a live dark-matter (DM) halo, and the initial conditions were generated using GalactICS (Kuijken & Dubinski 1995; Widrow &

Dubinski [2005]). The stellar disc follows an exponential profile with a mass of $3.73 \times 10^{10} M_\odot$, an initial scale length (R_d) of 2.3 kpc, and an initial scale height of 0.2 pc. The classical bulge follows the Hernquist profile (Hernquist [1990]), whose mass and scale length are $5.42 \times 10^9 M_\odot$ and 750 pc, respectively. The DM halo follows the Navarro–Frenk–White (NFW) profile (Navarro, Frenk & White [1997]), whose mass and scale radius are $8.68 \times 10^{11} M_\odot$ and 10 kpc, respectively. A more detailed model description can be found in Fujii et al. ([2019]).

The simulations were performed using the parallel GPU tree-code, BONSAI[1] (Bédorf, Gaburov & Portegies Zwart [2012]; Bédorf et al. [2014]) with a GPU cluster, Piz Daint.

The simulation was started from a disc without any structures. After ~ 2 Gyr, a bar started to form and continued to grow until ~ 5 Gyr. During the evolution, the bar slowed down with oscillations up to ~ 8 Gyr. Spiral structures also formed and are most prominent at ~ 5 Gyr. However, they faint at later times due to the dynamical heating of the disc. The simulation was continued up to 10 Gyr.

This simulation is one of the most highly resolved *N*-body simulations that we have performed. The numbers of particles of this models are 30 M, 208 M, and 4.9 B for the bulge, disc, and halo, and the same mass resolution is used for all the three components. This large number of particles enable us to perform a direct comparison of simulation results with observed data. A further advantage of this simulation is the high time resolution of the particle data output. The position- and velocity-snapshots of disc particles were stored every 9.76 Myr. We therefore can directly recover the actual orbits of individual stars from the snapshots.

2.2 Determination of the bar's pattern speed in the simulation

In this simulation, we determine the bar's pattern speed using the Fourier decomposition as was also done in Fujii et al. ([2019]). We divide the galactic disc into annuli with a width of 1 kpc and then Fourier decompose the disc's surface density in each annulus

$$\Sigma(R, \phi) = \sum_{m=0}^{\infty} A_m(R) \exp\{im[\phi - \phi_m(R)]\}, \tag{1}$$

where $A_m(R)$ and $\phi_m(R)$ are the m-th mode's amplitude and phase angle, respectively. We define $\phi_2(R)$ averaged in $R < 3$ kpc as the angle of the bar in the snapshot (see also Fujii et al. [2019]). We obtained the angle of the bar of the last 64 snapshots, which corresponds to $t = 9.38$–10 Gyr. Finally, the bar's pattern speed, Ω_b, is determined using the least squares fitting to $\phi_2(t) = \Omega_b t + \phi_{2,0}$, where $\phi_{2,0}$ is the angle of the bar in the first snapshot we used. The thus obtained pattern speed of the bar in the simulation is $\Omega_b = 46.12$ km s^{-1} kpc^{-1} = $1.53\Omega_{8\text{kpc}}$, where $\Omega_{8\text{kpc}}$ is the circular frequency at $R = 8$ kpc in our MW model. Recent studies such as Sanders et al. ([2019]) and Bovy et al. ([2019]) suggested a pattern speed of the Galactic bar of $\Omega_b = 41$ km s^{-1} kpc$^{-1} \simeq 1.4\Omega_0$, where Ω_0 is the circular velocity at the solar distance. The bar's pattern speed in our simulation is slightly higher than this value, but slower than that favoured by Dehnen ([2000])'s 2:1 OLR model for the Hercules stream ($\Omega_b \simeq 50$ km s^{-1} kpc$^{-1} \simeq 1.8\Omega_0$).

2.3 Distribution of simulated stars in velocity space

To study the origin of the Hercules stream, we begin by locating a Sun-like position in the simulated galactic disc. We take the last

---

snapshot of the simulations ($t = 10$ Gyr) and plot the velocity–space distribution of particles within 0.2 kpc from the 'Sun' and iterate over positions in the disc. The results are shown in Fig. 2. Note that we assume the position of the 'Sun' in the galactic mid-plane ($z = 0$) in the MW model.

At certain locations, we find a velocity–space structure similar to the one observed in *Gaia* DR2 (Gaia Collaboration et al. [2018b] and Fig. 1). These observational studies suggest that the Sun has a distance of $R_\odot = (8.178 \pm 13 \pm 22)$ kpc (Gravity Collaboration et al. [2019]) from the Galactic Centre and lies at an angle of $\phi_\odot = 27° \pm 2°$ (Wegg & Gerhard [2013]), $29° \pm 2°$ (Cao et al. [2013]), $24°$–$27°$ (Rattenbury et al. [2007]), and $20°$–$25°$ (Bissantz & Gerhard [2002]) with respect to the major axis of the Galactic bar. By analysing our simulations, we select a distance and position relative to the bar of $(R, \phi) = (8$ kpc$, 20°)$. This choice is based on the similarity of the structure observed in Fig. 1 and compared with the kaleidoscope of similar phase-space images in Fig. 2. The velocity–space map at $(R, \phi) = (8$ kpc$, 30°)$ also shows the Hercules-like stream, but it is most clearly identified in the map at $(R, \phi) = (8$ kpc$, 20°)$. The space-coordinates framed in red in Fig. 2 has the closest correspondence with the observed image. We then select this particular phase-space position as the one to represent the Sun in our simulations.

Fig. 3 is the enlarged figure of the velocity–space distribution at $(R, \phi) = (8$ kpc$, 20°)$ (same as the panel framed by a red rectangle in Fig. 2). A Hercules-like stream is located from $(v_R, v_\phi) \simeq (80, 200)$ km s^{-1} to $(v_R, v_\phi) \simeq (-60, 190)$ km s^{-1} in this figure. In addition, a Hat-like stream and a Horn-like structure are also seen from $(v_R, v_\phi) \simeq (50, 260)$ to $(v_R, v_\phi) \simeq (-50, 270)$ km s^{-1} and around $(v_R, v_\phi) = (-50, 220)$ km s^{-1}, respectively. Some other moving groups known from observations, such as the Hyades and Pleiades, cannot be clearly mapped to structures in the simulated MW model.

3 ORBIT ANALYSIS AND IDENTIFICATION OF RESONANTLY TRAPPED STARS

The key advantage of working with an *N*-body simulation is that resonances can be tested in live systems. The spiral structures and bars evolve with time in a live potential, which is not the case in static potential simulations. In such a time-dependent potential, stars in a resonance may not be able to stay stable in the resonance. In order to capture resonances in a live potential, the orbits of individual stellar orbits have to be followed in the live simulations.

To this aim, we thus use the snapshots of our *N*-body simulation and trace the orbits of the stars that we are interested in. We especially determine the orbital frequencies of the disc particles in order to classify the particles by their orbital characteristics such as resonances. For this purpose, we perform a frequency analysis of stellar orbits obtained from the *N*-body simulation with a following frequency measurement method used in Ceverino & Klypin ([2007]). Here, we detail upon the classification scheme used to identify stellar properties in our simulation.

First, we determine the radial frequency, Ω_R, using the Discrete Fourier Transformation (DFT) for $R(i)$, where $R(i)$ ($i = 1, \ldots, 64$) is a radial coordinate in the i-th snapshot. We employ a zero-padding technique for Fourier transforming: 960 zero points are added at the end of the data series. We then sample frequency space with 512 points between 0 and 315 km s^{-1} kpc^{-1}, whereby the upper bound is given by the Nyquist frequency. We identify a resonant Ω_R as a frequency that causes a local maximum in the Fourier spectrum: obviously, the local maximum indicates an overabundance of stars
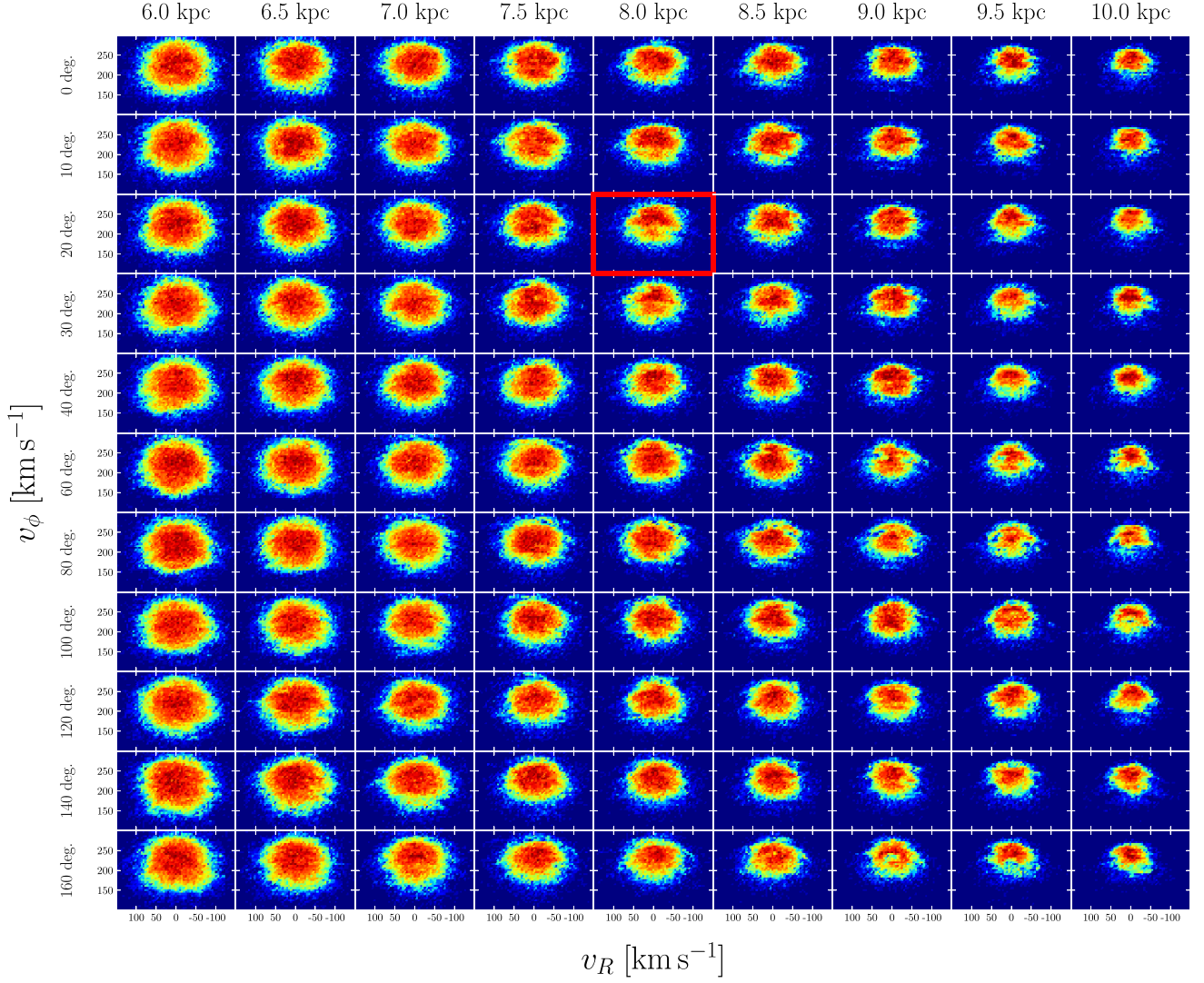
Figure 2. 2D histogram in v_R versus v_ϕ space at various positions in the disc at 10 Gyr. The distribution is for particles within 0.2 kpc from each position. In all panels, the bin size is set to $5 \times 5 \, (\mathrm{km\,s^{-1}})^2$. The panel for $(R, \phi) = (8 \, \mathrm{kpc}, 20°)$, corresponding to the solar neighbourhood, is framed by a red rectangle.

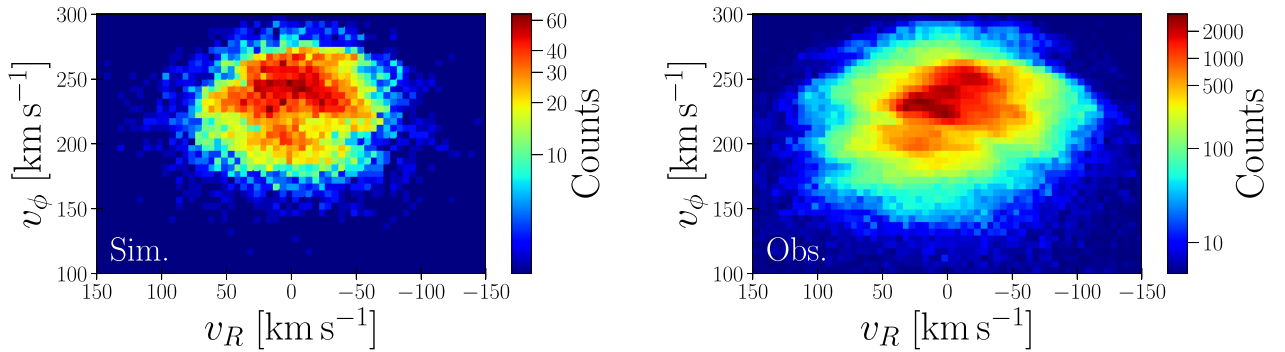**Figure 3.** Left-hand panel: Distribution of simulation particles in velocity space around $(R, \phi) = (8 \, \mathrm{kpc}, 20°)$. This is an enlargement of the panel framed by a red rectangle in Fig. 2. Right-hand panel: The same figure from *Gaia* DR2. The total number of the stars in the maps of the simulation and the observation are 13 303 and 345 152, respectively.
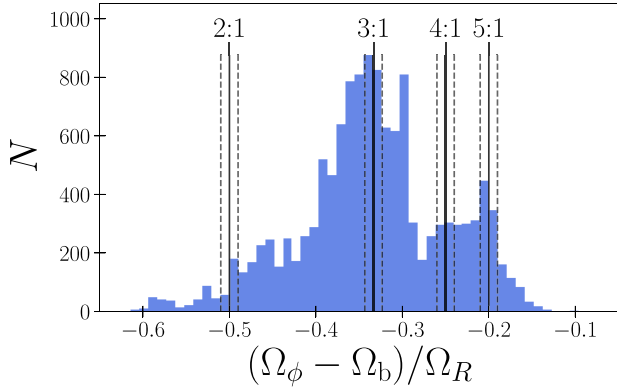
Figure 4. Orbital frequency ratios for the particles within $0.2\,\text{kpc}$ from $(R, \phi) = (8\,\text{kpc}, 20°)$. The four vertical solid lines indicate $(\Omega_\phi - \Omega_\text{b})/\Omega_R = $ -1/2, -1/3 -1/4, and -1/5, corresponding to the 2:1, 3:1, 4:1, and 5:1 resonances, respectively. Pairs of dashed lines beside solid lines indicate frequency ratios of $-1/2 \pm 0.01$, $-1/3 \pm 0.01$, $-1/4 \pm 0.01$, and $-1/5 \pm 0.01$, respectively. For each resonance, particles whose frequency ratios are between a dashed line pair are selected as resonantly trapped particles.

at this frequency. In contrast, the associated angular frequency Ω_ϕ is determined by a regression analysis instead of a Discrete Fourier Transform. From the snapshots, we collect per particle the series of measured angles $\phi(i)$ as a function of time $t(i)$, where i iterates over the 64 snapshots available. For each particle, this results in pairs $[t(i), \phi(i)]\,(i = 1, \ldots, 64)$ to which we fit the function $\phi = \Omega_\phi t + \phi_0$ using a least squares method. The resulting Least-Squares Estimator yields the angular frequency Ω_ϕ of the studied star.

In Fig. 4, we show the distribution of the frequency ratio $(\Omega_\phi - \Omega_\text{b})/\Omega_R$ for the particles within $0.2\,\text{kpc}$ from our 'Sun's' location at $(R, \phi) = (8\,\text{kpc}, 20°)$. Here, we use the bar's pattern speed (Ω_b) obtained from our simulations (see Section 2.2). The clearly visible statistically significant peaks in the distribution correspond to stars in resonances with the bar, whereas small fluctuations simply arise from binning. In Fig. 4, we indicate the positions of multiple OLRs as vertical solid lines. In the region that we assumed as the solar neighbourhood, we find at the four OLR of 2:1, 3:1, 4:1, and 5:1.

We assume that particles within a rage of ± 0.01 from the exact resonance frequency ratio are also in resonance; these are the two adjacent bins to the exact resonance frequency. We select these as resonant particles in the following analyses. As an example, for particles trapped in the 2:1 resonance, we select those whose frequency ratios are in the range of $-0.51 < (\Omega_\phi - \Omega_\text{b})/\Omega_R < -0.49$ which corresponds to the bins between the two vertical dashed lines next to the line of $(\Omega_\phi - \Omega_\text{b})/\Omega_R = -0.5$.

In order to confirm the validity of this selection procedure, we verify whether the selected particles are in resonant orbits. To verify the results of the Fourier analysis, we randomly select 100 particles from the various resonant areas and plot their orbits over time. By visually inspecting them, as the sub-sample of five cases for each of the orbital resonances, presented in Fig. 5, we confirm that except a few odd cases, all stars are on the appropriate resonance orbit. We show the panels that demonstrate this procedure for 100 different plotted orbits in the online material. All the orbits in Fig. 5 are shown in the rotating frame of the bar, which is represented by the grey ellipse in each panel. In this figure, the galaxy rotates clockwise. In this frame, the particles accordingly rotate counterclockwise as their angular frequencies are slower than the bar's pattern speed. Stars trapped in the m:1 resonances oscillate m times in the radial
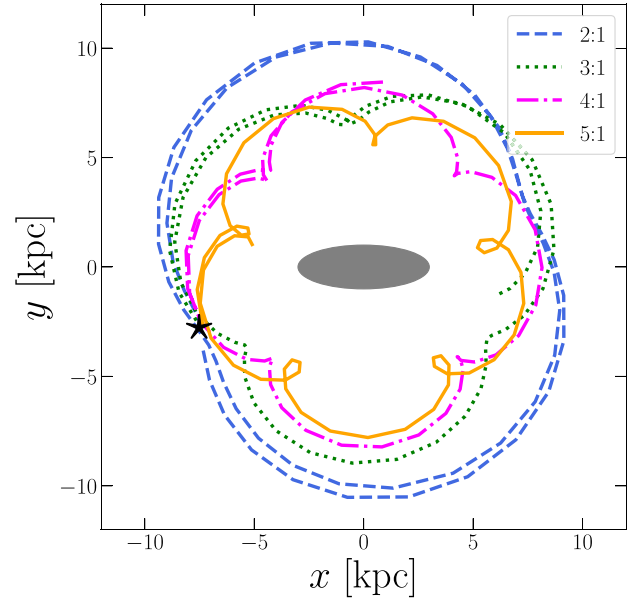

Figure 5. Examples of the orbits trapped in the bar resonances. The grey ellipse in the figure represents the bar orientation. The orbits are shown in the bar's rotating frame. The galaxy rotates clockwise, hence particles rotate counterclockwise in this frame.

direction while they circle the bar. Thus, we confirm that our method properly identifies stars in resonant orbits.

Note that naively, one would expect that orbits of the 2:1 resonance to align with the bar or to be perpendicular to it in the case of OLR. In our simulation, however, we find that the orbits in the 2:1 OLR are inclined with respect to the orientation of the bar as shown in the top five panels in Fig. 5. In other regions, however, particles which are exactly aligned with or perpendicular to the bar are dominant. In the region which we assumed as the solar neighbourhood, particles in inclined orbits are dominant. The reason is currently not clear, but this may be because the position we 'observed' is not exactly on the 2:1 OLR radius. Other possible reasons are spiral arms and/or the bar's slow-down.

Orbital radii decrease from lower to higher order resonances (from the top to the bottom in Fig. 5). This is more apparent in Fig. 6, in which we show four resonantly trapped orbits in a single frame. This is simply because higher order resonances have smaller guiding radii.

4 RESULTS FOR *GAIA* DR2

Using the orbit analysis of our simulation detailed upon in Section 3, we succeeded in identifying the simulation's bar pattern speed and the resonance type of stars trapped in resonant orbits. By now comparing to the *Gaia* data, we can thus use our simulation analysis to constrain the properties of the MW galaxy. The thus found implications for the origin of the Hercules stream are presented in Section 4.1 and constraints on the MW's bar pattern speed are presented in 4.2.

4.1 The origin of the Hercules stream from resonances

The *Gaia* DR2, the Hercules stream creates a prominent overdensity of stars in the v_R versus v_ϕ projection of the *Gaia* data (see Fig. 1). The recognition of this overdensity's trimodality (e.g. Ramos et al. 2018) is recent and requires an explanation. We here present the evidence
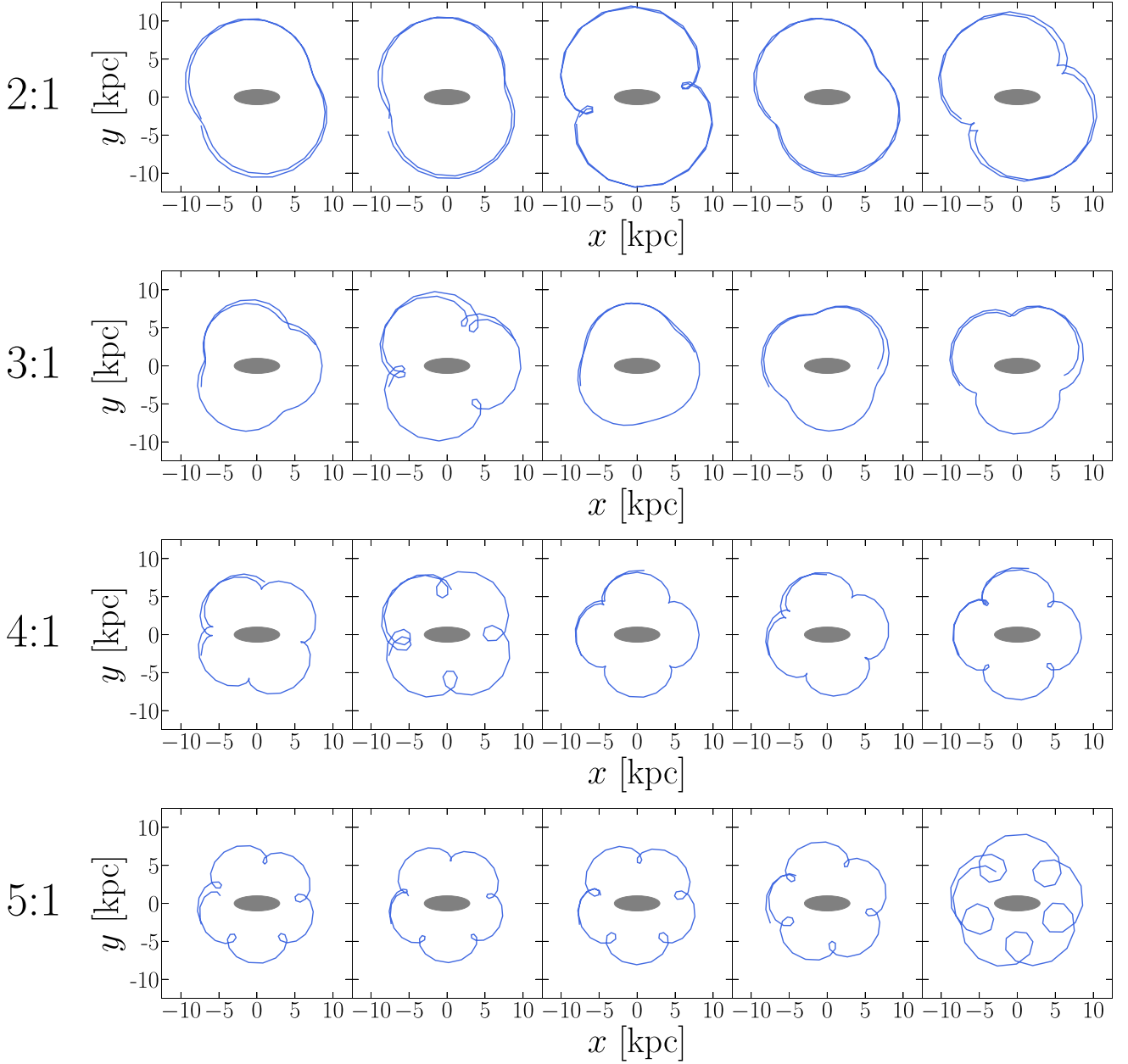
Figure 6. Resonantly trapped orbits in a single frame. The blue dashed, green dotted, magenta dash–dotted, and orange solid lines represent the 2:1, 3:1, 4:1, and 5:1 resonance orbits, respectively. In this figure, the galaxy rotates clockwise. The star symbol presents the position of the Sun in our model, $(R, \phi) = (8\,\mathrm{kpc}, 20°)$.

that stars trapped in resonant orbits will form such a trimodal stream structure.

This can be seen from the top panel of Fig. 7, where we over plot the position of particles in resonance in the velocity map (Fig. 3). In the bottom panel of the figure, we show the velocity map coloured by the fraction of particles in resonance in each bin. We find that between 60 and 100 per cent of all stars in the Hercules-like stream of our simulation are trapped in the 4:1 and 5:1 OLR. This implies that the stars within the Hercules stream (two streams at $v_\phi = 220$ and $200\,\mathrm{km\,s^{-1}}$) will also be dominated by resonantly trapped stars. Although the two resonantly trapped families are blurred in our velocity map of Fig. 3, these two streams light up and are clearly separated when classified by resonance type

in Fig. 7, thereby providing a natural explanation for multiple streams of *Gaia*'s observations of the Hercules stream.

In our simulations, stars trapped in the 2:1 OLR have velocities much higher than the rotation speed at the position of the Sun. This is because the guiding centre of the 2:1 OLR in our model is outer than 8 kpc. These stars appear to populate the area in phase space that was characterized by the 'hat' structure in the observation. Stars in the 3:1 OLR are distributed around the circular velocity at 8 kpc. Among the 3:1 OLR stars, those with $v_R < 0$ are part of the 'horn' structure.

The guiding-centre radius (R_g) for each OLR for our simulated model can be determined as we know the structure of the simulated galactic disc. The radial frequency under the epicycle approximation
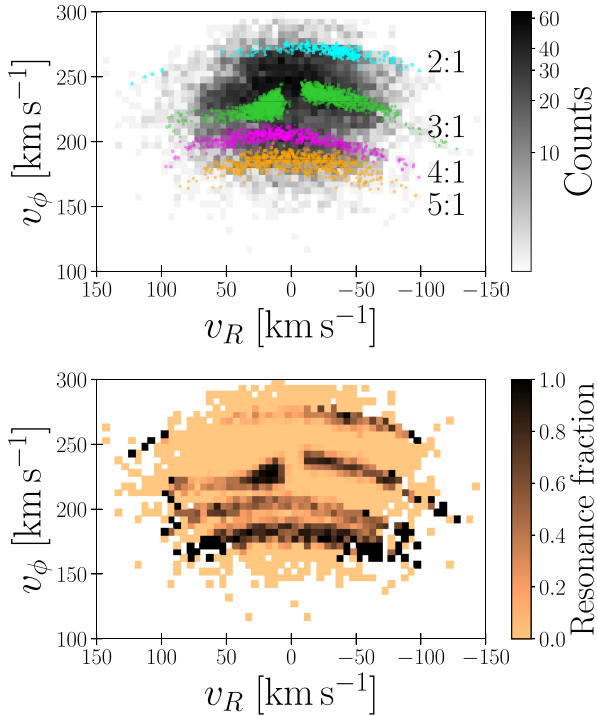
Figure 7. Top: Resonantly trapped particles in velocity space. The velocities of resonantly trapped particles are overplotted on the v_R versus v_ϕ plane in Fig. 3. Cyan, green, magenta, and orange dots represent particles trapped in the 2:1, 3:1, 4:1, and 5:1 resonances, respectively. Bottom: Colours indicate the fraction of the particles trapped in the 2:1, 3:1, 4:1, or 5:1 resonances in each bin.
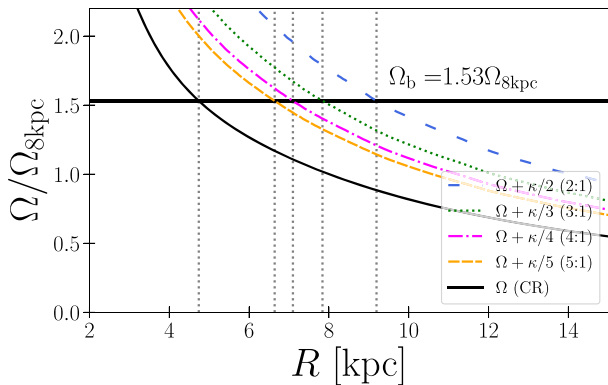

Figure 8. The orbital frequencies as functions of the galactic radius, R. Ω was determined from the velocity curve and $\Omega + \kappa/m$ (m =2, 3, 4, and 5) as expected within the epicycle approximation are plotted. The vertical axis is normalized by Ω_{8kpc}. The horizontal line indicates the bar's pattern speed and the vertical lines represent the guiding radii for the respective resonant orbits.

is given by Binney & Tremaine 2008

$$\kappa^2(R_g) = \left(R \frac{d\Omega^2}{dR} + 4\Omega^2 \right)_{R_g}. \tag{2}$$

Here, we calculate κ and Ω at each radius from the particle data of the *N*-body simulation. We also determine the circular frequency, Ω, by averaging the radial accelerations of particles in an annulus with a width of 50 pc at each radius. In Fig. 8, we show $\Omega + \kappa/m$ (m =2, 3, 4, and 5) and Ω as functions of R. The horizontal line in Fig. 8 indicates

the pattern speed of the bar. The radii at which the line intersects with the frequency curves correspond to the guiding-centre radii for the 2:1, 3:1, 4:1, 5:1, and the corotation resonances. In our model of the MW, the Sun, at a distance of ∼8 kpc from the Galactic Centre, is close to the 3:1 OLR. It is then not surprising that this resonance is dominant in the local stellar population.

4.2 The MW's bar pattern speed

When projecting the *Gaia* DR2 data into the R–v_ϕ plane, a series of ridges appear over a wide range of R (Antoja et al. 2018; Kawata et al. 2018; Ramos et al. 2018). Although the origin of these structures is still in debate, previous studies (e.g. Monari et al. 2017b, 2019a; Fragkoudi et al. 2019; Barros et al. 2020) have discussed that these ridges may originate from resonances, while other studies have suggested perturbations by a satellite galaxy such as the Sagittarius dwarf (Khanna et al. 2019; Laporte et al. 2019) or by winding transient spiral structure (Hunt et al. 2018, 2019). In this section, we study the relation between the observed ridges in *Gaia* DR2 and resonances in our simulated MW model: by projecting our simulated and classified stars into the R–v_ϕ plane, we can directly compare to the same projection of the *Gaia* DR2 data. If the stars classified by resonance type align with the observed ridges, then this provides compelling evidence that these ridges are indeed caused by resonantly trapped stars.

In Fig. 9, we show the distributions of stars in the R–v_ϕ plane as it arises in our simulated MW model (left-hand column) and in the *Gaia* DR2 (right-hand column). The top panels show 2D histograms of particles within 2 kpc from the Sun [$(R, \phi) = (8\,\text{kpc}, 20°)$, in our model]. This panel reveals a selection effect caused by *Gaia*'s measurement uncertainties: due to us having selected stars with relative parallax error below 10 per cent the right-hand panel displays systematically fewer stars in approximately concentric rings around the Sun's position at 8.2 kpc. Visually, this causes the smaller extend of the red area in the right-hand panel. We expected, however, that our analysis is robust with respect to this selection effect: it implies that fewer stars make it into our DR2 projection than into the projection of our simulation, but those stars that are selected are not systematically biased.

The middle panels show the mean v_R values in the respective bins in the top panels. In order to make this figure, we selected stars from the *Gaia* DR2 catalogue whose relative errors in parallaxes are less than 10 per cent, and whose errors in radial velocities are less than 5 km s^{-1}. Their distances from the Galactic mid-plane are less than 0.2 kpc and their distances from the Sun are less than 2 kpc. The total number of stars in this sample is 2289 755. We assume that the distance of the Sun from the Galactic Centre is $R_0 = 8.2$ kpc and that the distance of the Sun from the Galactic mid-plane is about $z_0 = 25$ pc, whereby the velocity of the Sun with respect to the Local Standard of Rest (LSR) is about $(U_\odot, V_\odot) = (10, 11)$ km s^{-1}, and the circular velocity at $R = R_0$ of $\Theta_0 = 238$ km s^{-1} (Bland-Hawthorn & Gerhard 2016).

In the middle right-hand panel in Fig. 9, we can identify several streams, or ridges, in the *Gaia* data. For convenience, we refer to ridges with $v_R > 0$ as 'red' and $v_R < 0$ as 'blue'. From top to bottom, red ridges alternate with blue ridges. Amongst these, two red ridges of $v_R > 0$ are located at $v_\phi \sim 200$ km s^{-1} and $v_\phi \sim 180$ km s^{-1} at 8 kpc, are associated with the Hercules stream. In the middle panel, our simulation is shown on the left-hand side. It shows ridges similar to those observed in the *Gaia* data (middle panel on the right-hand side). In our previous discussion, we argued that the Hercules-like stream in our MW model corresponds to a ridge from $(R, v_\phi) \simeq$
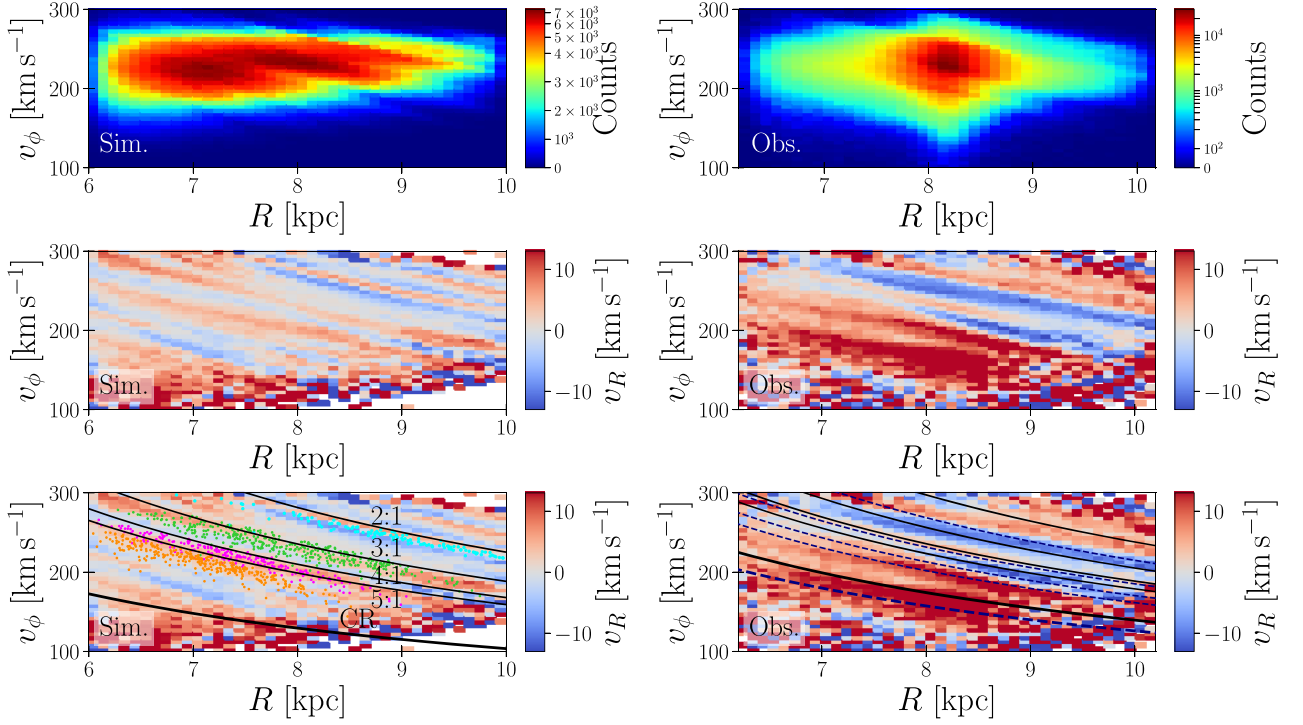
Figure 9. Left-hand panels: Phase-space structures in the R versus v_ϕ space from the MW simulation. Right-hand panels: Counterparts from *Gaia* DR2. Top: Colours indicate the number counts in each bin. Middle: Colours indicate the mean v_R in each bin. Bottom: Same as middle panels, but with curves of constant angular momentum overplotted. From the top to bottom curves, they correspond to the angular momenta of the circular orbits at a resonant radius of the 2:1, 3:1, 4:1, 5:1 OLR, and CR. Solid and dashed curves in the bottom right-hand panel correspond to a bar's pattern speed of $\Omega_b = 1.4\Omega_0 \simeq 40\,\mathrm{km\,s^{-1}\,kpc^{-1}}$ or $\Omega_b = 1.55\Omega_0 \simeq 45\,\mathrm{km\,s^{-1}\,kpc^{-1}}$, respectively. Dots in the bottom left-hand panel indicate positions of particles trapped in each of the resonances. The colours are the same as those in Fig. 7.

(6 kpc, 250 km s^{-1}) to $(R, v_\phi) \simeq (9\,\mathrm{kpc}, 180\,\mathrm{km\,s^{-1}})$. This ridge, eventually branches into two separate structures at around 8 kpc.

In order to study the relation between the resonances and ridges in our simulation, we overplot the positions of particles in the resonances in the bottom left-hand panel of Fig. 9. We here randomly sample 5000 particles within 2 kpc from $(R, \phi) = (8\,\mathrm{kpc}, 20°)$ and extract resonant particles from them as we do in Section 3. In addition, we plot curves of constant angular momentum ($L_z = Rv_\phi$) in the figure. These correspond to the angular momenta of the circular orbits at the resonance radii determined in Fig. 8. As discussed in studies such as Ramos et al. (2018) and Quillen et al. (2018), resonant orbits approximately follow constant L_z curves if their radial oscillations are small.

The overplotting reveals that both the resonant particles and constant L_z curves follow the ridges. While Monari et al. (2019a) showed that the constant L_z curves are blue ridges ($v_R < 0$) for 2:1, 3:1, and 4:1 resonances according to their Fig. 6, our L_z curves fall just between red ($v_R > 0$) and blue ridges. In addition, we find that the resonant particles are always distributed below the constant L_z curves in R–v_ϕ map. This arises due to their radial oscillations not being negligible. Orbits in a resonance follow a line in L_z versus J_R space where J_R is a radial action (see Fig. 4 in Binney 2018). As the resonant lines have negative slopes, if resonant orbits J_R values are large, their L_z values are smaller than those of the circular orbits ($J_R = 0$).

Turning to the *Gaia* data, the ridges seem to trace the constant angular momentum lines also in our MW's data. The solid curves in the bottom right-hand panel of Fig. 9 represent the angular momenta

of the resonances for the bar's pattern speed of $\Omega_b = 1.4\Omega_0$, which is suggested by Sanders et al. (2019) and Bovy et al. (2019). We also present the same ones but for $\Omega_b = 1.55\Omega_0$, which is the pattern speed in our simulation. In order to determine the radii of the resonances and corresponding angular momenta, we assume a flat rotation curve of $v_c = 238\,\mathrm{km\,s^{-1}}$.

Consider that the top red ridge corresponds to the 2:1 OLR, the full curve (at $\Omega_b = 1.4\Omega_0$) then is close to the relation between the colour and constant L_z curve as shown in our simulation (the curve is located just above the red ridge). However, with $\Omega_b = 1.4\Omega_0 = 40\,\mathrm{km\,s^{-1}\,kpc^{-1}}$, there are no OLR around the Hercules stream, but the corotation resonance is located at the lowest value of v_ϕ of the Hercules stream. Accordingly, if we assume a higher pattern speed, i.e. $\Omega_b = 1.55\Omega_0 = 45\,\mathrm{km\,s^{-1}\,kpc^{-1}}$, the 2:1 resonance is located slightly below the top red ridge, but the relation between the resonances and ridges for the 4:1 and 5:1 resonances looks similar to that seen in our simulations. In both pattern speeds, the pronounced red ridge near the bottom which we identify with the third Hercules stream, correspond to the corotation resonance. We find the same phenomena in our simulation, but without the stars in corotation resonance. The latter is a consequence if the relatively low-resolution of our simulations and the fact that in the *Gaia* data the corotation resonance is closer to the Sun than in our simulations. This is a consequence of our models not perfectly matching to the real MW galaxy. Thus, our comparison between the *Gaia* data and our simulation suggest that the pattern speed of the MW's bar is relatively slow, with $\Omega_b = 1.4$–$1.55\Omega_0$ which corresponds to 40–45 km s^{-1} kpc^{-1}

5 SUMMARY

We have analysed a finely resolved *N*-body simulation of a MW-like galaxy obtained in Fujii et al. (2019) in order to investigate the origins of the phase-space structures in the MW galaxy as observed by *Gaia*. We investigated the distribution of particles in the v_R–v_ϕ plane by iterating over multiple positions in the disc. This revealed a Hercules-like stream around $(R, \phi) = (8\,\mathrm{kpc}, 20°)$ in our simulation, as is also known from the actual solar neighbourhood. From a spectral analysis of stellar orbits, we found mainly four resonances, namely the 2:1, 3:1, 4:1, and 5:1 resonances around there. The observed structures in the v_R–v_ϕ plane, can be explained by stars being trapped in the 4:1 and 5:1 OLRs. In our simulations, these resonances give rise to structures similar to those observed in the actual Hercules stream. Our results therefore favour that the Hercules stream is composed out of stars trapped in the 4:1 and 5:1 OLR and CR, which would also explain its trimodal structure as revealed by *Gaia* DR2. In addition, the stars in the 2:1 and 3:1 OLR match to the 'hat' and 'horn' structures, respectively.

We further compared the distribution of stars in the R–v_ϕ plane in our simulation with that obtained from the *Gaia* data. Particles identified to be in resonance in our simulation follow ridges in the R–v_ϕ plane. Similar ridges have also been found in the *Gaia* data and matching the observed ridges to resonances, our results suggest a relatively low pattern speed of the MW's bar, namely $\Omega_b = 1.4$–$1.55\Omega_0$, which corresponds to 40–$45\,\mathrm{km\,s^{-1}\,kpc^{-1}}$. This is consistent with recent studies (e.g. Bovy et al. 2019; Sanders et al. 2019).

In contrast to test particle models using static potentials, *N*-body models have some difficulties when comparing the results with observational data due to the time-dependence of the bar and spiral arms. Fujii et al. (2019) showed that v_R–v_ϕ maps obtained from *N*-body simulations change with time. This is a natural consequences of dynamic spiral arms (e.g. Sellwood & Carlberg 1984; Baba et al. 2013). In fact, Hunt et al. (2018, 2019) discussed phase mixing by dynamic transient spiral arms, which in combination with bar resonances, creates a velocity–space distribution similar to what is seen in observations (see also De Simone, Wu & Tremaine 2004). Furthermore, the evolution of the bar can also affect the stellar velocity–space distribution. Recently, Chiba, Friske & Schönrich (2019) showed that stars trapped in the resonances of the bar are dragged in the phase space when the bar slows down using secular perturbation theory and test particle simulations (see also Weinberg 1994; Halle et al. 2018). This can also cause the formation of a Hercules-like structure. We will discuss the time dependence of the velocity distribution, caused by the dynamical evolution of spiral arms and bar in fully self-consistent *N*-body simulations, in a forthcoming paper.

DATA AVAILABILITY

The data underlying this article will be shared on reasonable request to the corresponding author.

REFERENCES

Aguerri J. A. L., Debattista V. P., Corsini E. M., 2003, MNRAS, 338, 465
Aguerri J. A. L. et al., 2015, A&A, 576, A102
Antoja T. et al., 2014, A&A, 563, A60
Antoja T. et al., 2018, Nature, 561, 360
Baba J., Asaki Y., Makino J., Miyoshi M., Saitoh T. R., Wada K., 2009, ApJ, 706, 471
Baba J., Saitoh T. R., Wada K., 2013, ApJ, 763, 46
Barros D. A., Pérez-Villegas A., Lépine J. R. D., Michtchenko T. A., Vieira R. S. S., 2020, ApJ, 888, 75
Bédorf J., Gaburov E., Portegies Zwart S., 2012, J. Comput. Phys., 231, 2825
Bédorf J., , Gaburov E., Fujii M. S., Nitadori K., Ishiyama T., Portegies Zwart S., 2014, Proc. International Conference for High Performance Computing, Networking, Storage and Analysis. SC '14. IEEE Press, NJ, p. 54
Binney J., 2018, MNRAS, 474, 2706
Binney J., 2020, MNRAS, 495, 895
Binney J., Tremaine S., 2008, Galactic Dynamics, 2nd edn, Princeton Univ. Press, Princeton
Bissantz N., Gerhard O., 2002, MNRAS, 330, 591
Bland-Hawthorn J., Gerhard O., 2016, ARA&A, 54, 529
Bovy J., Leung H. W., Hunt J. A. S., Mackereth J. T., García-Hernández D. A., Roman-Lopes A., 2019, MNRAS, 490, 4740
Cao L., Mao S., Nataf D., Rattenbury N. J., Gould A., 2013, MNRAS, 434, 595
Ceverino D., Klypin A., 2007, MNRAS, 379, 1155
Chiba R., Friske J. K. S., Schönrich R., 2019, preprint (arXiv:1912.04304)
Clarke J. P., Wegg C., Gerhard O., Smith L. C., Lucas P. W., Wylie S. M., 2019, MNRAS, 489, 3519
D'Onghia E., L. Aguerri J. A., 2020, ApJ, 890, 117
D'Onghia E., Vogelsberger M., Hernquist L., 2013, ApJ, 766, 34
De Simone R., Wu X., Tremaine S., 2004, MNRAS, 350, 627
Dehnen W., 1998, AJ, 115, 2384
Dehnen W., 1999, ApJ, 524, L35
Dehnen W., 2000, AJ, 119, 800
Eggen O. J., 1971, PASP, 83, 762
Eggen O. J., 1978, ApJ, 222, 203
ESA ed., 1997, ESA SP-1200: The HIPPARCOS and TYCHO catalogues, ESA, Noordwijk
Fragkoudi F. et al., 2019, MNRAS, 488, 3324
Fujii M. S., Baba J., Saitoh T. R., Makino J., Kokubo E., Wada K., 2011, ApJ, 730, 109
Fujii M. S., Bédorf J., Baba J., Portegies Zwart S., 2019, MNRAS, 482, 1983
Fux R., 2001, A&A, 373, 511
Gaia Collaboration et al., 2016, A&A, 595, A1
Gaia Collaboration et al., 2018a, A&A, 616, A1
Gaia Collaboration et al., 2018b, A&A, 616, A11

Grand R. J. J., Kawata D., Cropper M., 2012a, MNRAS, 421, 1529

Grand R. J. J., Kawata D., Cropper M., 2012b, MNRAS, 426, 167

Gravity Collaboration et al., 2019, A&A, 625, L10

Halle A., Di Matteo P., Haywood M., Combes F., 2018, A&A, 616, A86

Hattori K., Gouda N., Tagawa H., Sakai N., Yano T., Baba J., Kumamoto J., 2019, MNRAS, 484, 4540

Hernquist L., 1990, ApJ, 356, 359

Hunt J. A. S., Bovy J., 2018, MNRAS, 477, 3945

Hunt J. A. S., Hong J., Bovy J., Kawata D., Grand R. J. J., 2018, MNRAS, 481, 3794

Hunt J. A. S., Bub M. W., Bovy J., Mackereth J. T., Trick W. H., Kawata D., 2019, MNRAS, 490, 1026

Kalnajs A. J., 1991, in Sundelius B., ed., Dynamics of Disc Galaxies, Göteborgs Univ., Göteborgs, p. 323

Kawata D., Baba J., Ciucă I., Cropper M., Grand R. J. J., Hunt J. A. S., Seabroke G., 2018, MNRAS, 479, L108

Khanna S. et al., 2019, MNRAS, 489, 4962

Khoperskov S., Di Matteo P., Gerhard O., Katz D., Haywood M., Combes F., Berczik P., Gomez A., 2019, A&A, 622, L6

Kuijken K., Dubinski J., 1995, MNRAS, 277, 1341

Kushniruk I., Bensby T., Feltzing S., Sahlholdt C. L., Feuillet D., Casagrande L., 2020, A&A, 638, A154

Laporte C. F. P., Minchev I., Johnston K. V., Gómez F. A., 2019, MNRAS, 485, 3134

Li Z., Gerhard O., Shen J., Portail M., Wegg C., 2016, ApJ, 824, 13

Li Z.-Y., Shen J., 2020, ApJ, 890, 85

Michtchenko T. A., Lépine J. R. D., Barros D. A., Vieira R. S. S., 2018, A&A, 615, A10

Minchev I., Nordhaus J., Quillen A. C., 2007, ApJ, 664, L31

Minchev I., Boily C., Siebert A., Bienayme O., 2010, MNRAS, 407, 2122

Monari G., Famaey B., Siebert A., Duchateau A., Lorscheider T., Bienaymé O., 2017a, MNRAS, 465, 1443

Monari G., Kawata D., Hunt J. A. S., Famaey B., 2017b, MNRAS, 466, L113

Monari G., Famaey B., Fouvry J.-B., Binney J., 2017c, MNRAS, 471, 4314

Monari G., Famaey B., Siebert A., Wegg C., Gerhard O., 2019a, A&A, 626, A41

Monari G., Famaey B., Siebert A., Bienaymé O., Ibata R., Wegg C., Gerhard O., 2019b, A&A, 632, A107

Navarro J. F., Frenk C. S., White S. D. M., 1997, ApJ, 490, 493

Pérez-Villegas A., Portail M., Wegg C., Gerhard O., 2017, ApJ, 840, L2

Perryman M. A. C. et al., 1997, A&A, 500, 501

Portail M., Gerhard O., Wegg C., Ness M., 2017, MNRAS, 465, 1621

Quillen A. C. et al., 2018, MNRAS, 478, 228

Ramos P., Antoja T., Figueras F., 2018, A&A, 619, A72

Rattenbury N. J., Mao S., Sumi T., Smith M. C., 2007, MNRAS, 378, 1064

Sanders J. L., Smith L., Evans N. W., 2019, MNRAS, 488, 4552

Sellwood J. A., Carlberg R. G., 1984, ApJ, 282, 61

Sellwood J. A., Sparke L. S., 1988, MNRAS, 231, 25P

Sormani M. C., Binney J., Magorrian J., 2015, MNRAS, 454, 1818

Trick W. H., Coronado J., Rix H.-W., 2019, MNRAS, 484, 3291

Wegg C., Gerhard O., 2013, MNRAS, 435, 1874

Wegg C., Gerhard O., Portail M., 2015, MNRAS, 450, 4050

Weinberg M. D., 1994, ApJ, 420, 597

Widrow L. M., Dubinski J., 2005, ApJ, 631, 838

SUPPORTING INFORMATION

Supplementary data are available at *MNRAS* online.

orbits_100_21
orbits_100_31
orbits_100_41
orbits_100_51

Please note: Oxford University Press is not responsible for the content or functionality of any supporting materials supplied by the authors. Any queries (other than missing material) should be directed to the corresponding author for the article.

This paper has been typeset from a TeX/LaTeX file prepared by the author.